

The Role of Pore Size and Structure on the Thermal Stability of Gold Nanoparticles within Mesoporous Silica

Mangesh T. Bore,[†] Hien N. Pham,[†] Elise E. Switzer,[†] Timothy L. Ward,[†]
Atsushi Fukuoka,[‡] and Abhaya K. Datye^{*,†}

Department of Chemical and Nuclear Engineering and Ceramic and Composite Materials Center,
University of New Mexico, Albuquerque, New Mexico 87131, and Catalysis Research Center,
Hokkaido University, Sapporo 001-0021, Japan

Received: September 9, 2004; In Final Form: November 18, 2004

Highly dispersed gold particles (<2 nm) were synthesized within the pores of mesoporous silica with pore sizes ranging from 2.2 to 6.5 nm and different pore structures (2D-hexagonal, 3D-hexagonal, and cubic). The catalysts were reduced in flowing H₂ at 200 °C and then used for CO oxidation at temperatures ranging from 25 to 400 °C. The objective of this study was to investigate the role of pore size and structure in controlling the thermal sintering of Au nanoparticles. Our study shows that sintering of Au particles is dependent on pore size, pore wall thickness (strength of pores), and pore connectivity. A combination of high-resolution TEM/STEM and SEM was used to measure the particle size distribution and to determine whether the Au particles were located within the pores or had migrated to the external silica surface.

Introduction

Metal particles deposited on oxide supports are used extensively as heterogeneous catalysts. By using a suitable combination of active metal phases and supports, the catalysts are designed for high activity, selectivity, and mechanical strength. However, catalysts undergo deactivation, with poisoning, fouling, sintering, and volatilization being some of the common reasons for loss of catalyst activity.¹ For supported metal catalysts, sintering of metal particles is a major cause of catalyst deactivation. The rate and extent of sintering of supported metals depend on temperature, atmosphere, support, promoter, and metal. It is thought that the porosity of the support can play an important role in controlling sintering of metal particles.^{2,3} Richardson et al.² studied the effect of pore size on sintering of Ni/Al₂O₃ catalysts. They concluded that the size of the pores was an important variable controlling the final particle size in the sintered catalyst. Because the pores in alumina represent voids between primary oxide particles, there are a range of pore sizes and differing pore shapes. To study explicitly the role of pore size on sintering of supported metal particles, it would be desirable to work with supports having pores of uniform size and shape, preferably well ordered. In this regard, surfactant-templated mesoporous silica^{4–6} is a promising support material.

Mesoporous silicas having ordered, uniform pore sizes and structure have been extensively studied over the past 15 years.^{7,8} These silica materials can be prepared with various pore sizes and pore arrangements, for example, 2D-hexagonal, 3D-hexagonal, and cubic. In the 2D-hexagonal pore structure, the pores are one-dimensional and terminate on the particle surface. In such a pore structure, we can imagine that metal particles within a given pore can only interact with other particles in the same pore, with no possible interactions between neighboring

pores. In contrast, the 3D-hexagonal and cubic pore structures have interconnected pores, so the metal particles do not have to come out of the solid to interact with particles in neighboring pores. By depositing uniformly sized metal particles inside the pores of mesoporous silica, we can therefore study more clearly the role of pore size, pore structure, and connectivity and the ultimate impact on the thermal sintering of metal particles in supported catalysts.

One limitation of mesoporous silica for thermal sintering studies lies in its low hydrothermal stability at elevated temperatures.^{9,10} The pores of mesoporous silica reportedly collapse at temperatures above 500 °C. Hence, sintering studies must be performed at temperatures lower than 500 °C. Gold nanoparticles supported on silica show rapid sintering at 200–400 °C.¹¹ Hence, we have studied gold nanoparticles deposited within mesoporous silica to elucidate the role of pore size and pore structure on the rate of thermal sintering. It is known that gold nanoparticles supported on oxide supports show high reactivity for CO oxidation at low temperature, but only when the Au particles are very small (<5 nm).¹² Hence, the CO oxidation reaction serves as a suitable probe for the reactivity of these Au/mesoporous silica samples. Our study shows that sintering of Au particles is dependent on pore size, pore wall thickness, that is, strength of pores, as well as pore connectivity. For mesoporous silicas with similar pore sizes, the degree of sintering was greater for 3D-hexagonal and cubic pore structures as compared to the 2D-hexagonal pore structure. The final particle size increased with pore size. However, sintering can be controlled only if the pore walls are strong enough to immobilize the particles trapped inside the pores. In the present work, Au particles appear to grow by destroying the pore walls in the immediate vicinity of the metal particles.

Experimental Section

Synthesis of Mesoporous Silica. The MCM-41 was prepared by using CTAB as surfactant and sodium silicate as silica source. The molar ratio of the precursor solution was 3.4SiO₂:1-

* Corresponding author. Phone: (505) 277-0477. Fax: (505) 277-5433. E-mail: datye@unm.edu.

[†] University of New Mexico.

[‡] Hokkaido University.

CTAB:286H₂O. The surfactant was first dissolved in water. Sodium silicate was added to this surfactant solution. The pH of the solution was adjusted to 10 with 1 N nitric acid. The mixture was then transferred to a polypropylene bottle and kept in a water bath under static condition for 8 h at 80 °C. The mixture was then cooled to room temperature and kept at room temperature for 15 h. The powder collected was washed with water and vacuum-dried. The powder was calcined at 500 °C for 12 h in air to remove the surfactant.

SBA-15, SBA-11, and SBA-12 were synthesized using the method developed by Zhao et al.⁵ The sample labeled SBA-15/2 was prepared using the same precursor solution as that used for SBA-15, but the mixture was kept at 35 °C for 20 h, and then at 80 °C for 8 h, followed by 35 °C for 15 h. The higher temperature allowed us to obtain larger sized pores while keeping the same pore structure. HMM-2 was synthesized by the method developed by Inagaki et al.⁶

Gold Deposition on Mesoporous Silica. We have used the amine functionalization method^{13,14} to deposit gold inside the pores of mesoporous silica. Because the silica surface is negatively charged, functionalizing the surface with the amine facilitates adsorption of the (HAuCl₄)⁻ precursor. It is possible to mix the organic amine during the silica precipitation step, but we found this led to silica that was not well ordered. Hence, we used a two-step method, where mesoporous silica was first synthesized and next the preformed silica was treated with 3-aminopropyltrimethoxysilane for 24 h, washed in DI water, and vacuum-dried. After amine functionalization, the samples were labeled as NH₂-mesoporous silica, for example, NH₂-MCM-41. The BJH pore sizes reported for these mesoporous silica samples are after the amine functionalization. This amine-functionalized silica powder was then mixed with an aqueous hydrogen tetrachloroaurate hydrate solution (pH 7, adjusted with 1 M sodium hydroxide) to achieve a nominal gold loading of 5 wt %. After contacting the Au precursor for 24 h, the excess was washed off with DI water, and then vacuum-dried for 24 h. At this stage, samples were labeled Au-NH₂-mesoporous silica-as prepared, for example, Au-NH₂-MCM41-as prepared. The powder was then reduced at 200 °C for 2 h in flowing hydrogen, heating from room temperature at a ramp rate of 0.73 °C/min. After reduction, the samples were labeled Au-NH₂-mesoporous silica-Reduced, for example, Au-NH₂-MCM41-Reduced.

Reactivity Measurements. The reactivity measurements were performed with 20% CO and 10% O₂ and the balance helium at a total pressure of 670 Torr (atmospheric pressure in Albuquerque). The as-prepared samples did not show any reactivity for CO oxidation at room temperature. After reduction in flowing H₂ at 200 °C, we were able to detect CO oxidation activity. The reactivity was measured at temperatures from room temperature up to 400 °C at 50 °C intervals. These measurements were repeated for a total of three heating and cooling cycles, indicating that the results shown here are reproducible. After reaction, the samples were removed for examination by electron microscopy. These samples were labeled Au-NH₂-mesoporous silica-After Reaction, for example, Au-NH₂-MCM41-After Reaction.

Characterization. X-ray powder diffraction (XRD) patterns were obtained on a Scintag PAD-V diffractometer. Adsorption isotherms of nitrogen were carried out on a Micromeritics Gemini 2360 analyzer. HAADF (higher angle annular dark field) scanning transmission electron microscopy (STEM) images were obtained on a JEOL 2010F, 200 kV microscope. High-resolution

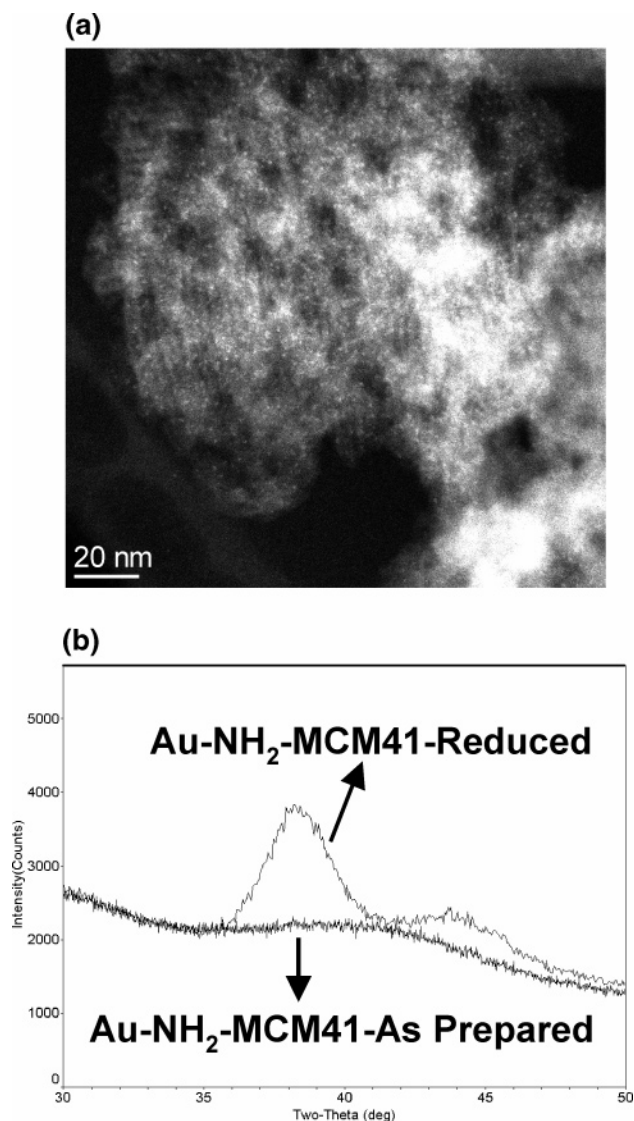


Figure 1. (a) HAADF (higher angle annular dark field) scanning transmission electron microscopy (STEM) image of the sample Au-NH₂-MCM41-As prepared. (b) XRD patterns of the samples Au-NH₂-MCM41-As prepared and Au-NH₂-MCM41-Reduced.

scanning electron microscopy (SEM) images were obtained on a Hitachi S-5200 microscope.

Results

The method of amine functionalization allows us to prepare highly dispersed Au in the mesoporous silica. The HAADF STEM image of the as-prepared MCM-41 (Figure 1a) shows well-dispersed Au nanoparticles ~1 nm in diameter. Also shown is an XRD pattern of this sample (Figure 1b) with no Au peak visible. The XRD data confirm that the particles are too small to be detected (<2 nm) due to the broadness of the XRD peaks. The image in Figure 1a is representative of all samples in their as-prepared state, where Au nanoparticles of ~1 nm in size can be seen by STEM HAADF, while no Au peak is seen by XRD. Figure 2 shows the HAADF STEM images of these samples after reduction at 200 °C for 2 h, while Figure 3 shows the images after three reaction cycles at temperatures ranging from room temperature to 400 °C. The average particle sizes are summarized in Table 1. From STEM images, an average particle size is calculated by measuring approximately 300 particles using Digital Micrograph software. The average particle size is

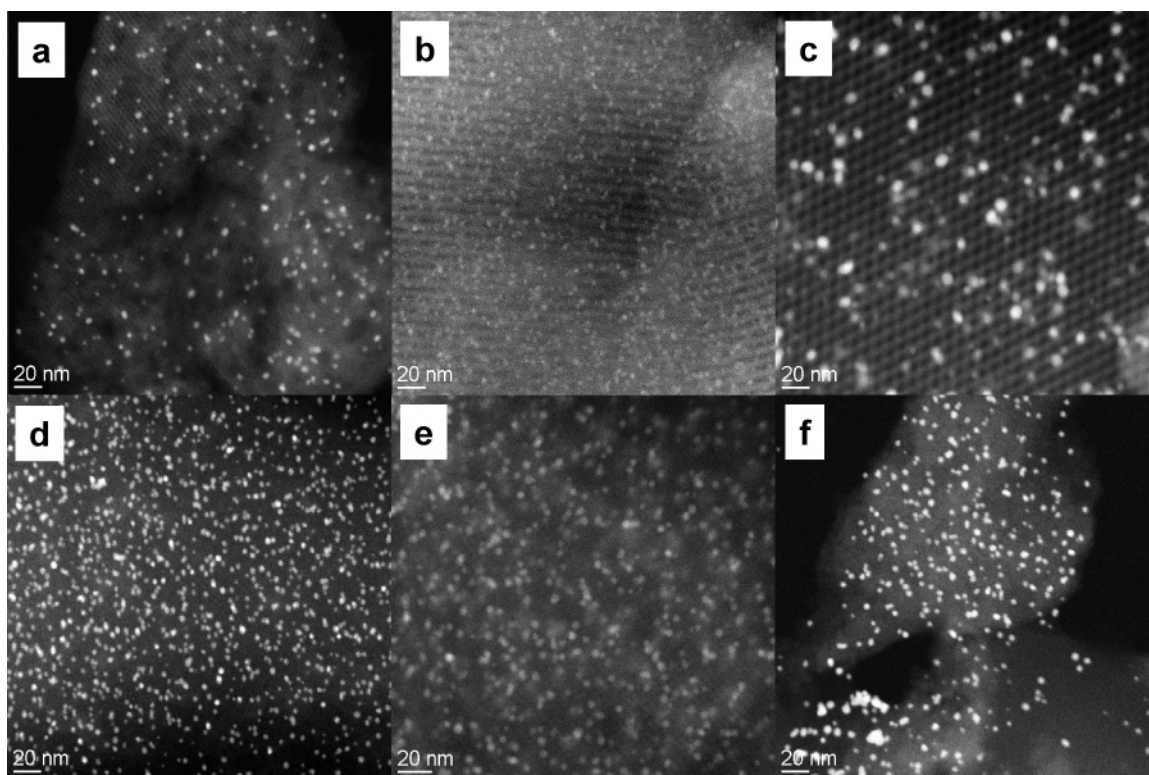


Figure 2. HAADF STEM images of samples after reduction at 200 °C for 2 h in flowing hydrogen. (a) MCM-41, (b) SBA-15, (c) SBA-15/2, (d) HMM-2, (e) SBA-12, and (f) SBA-11.

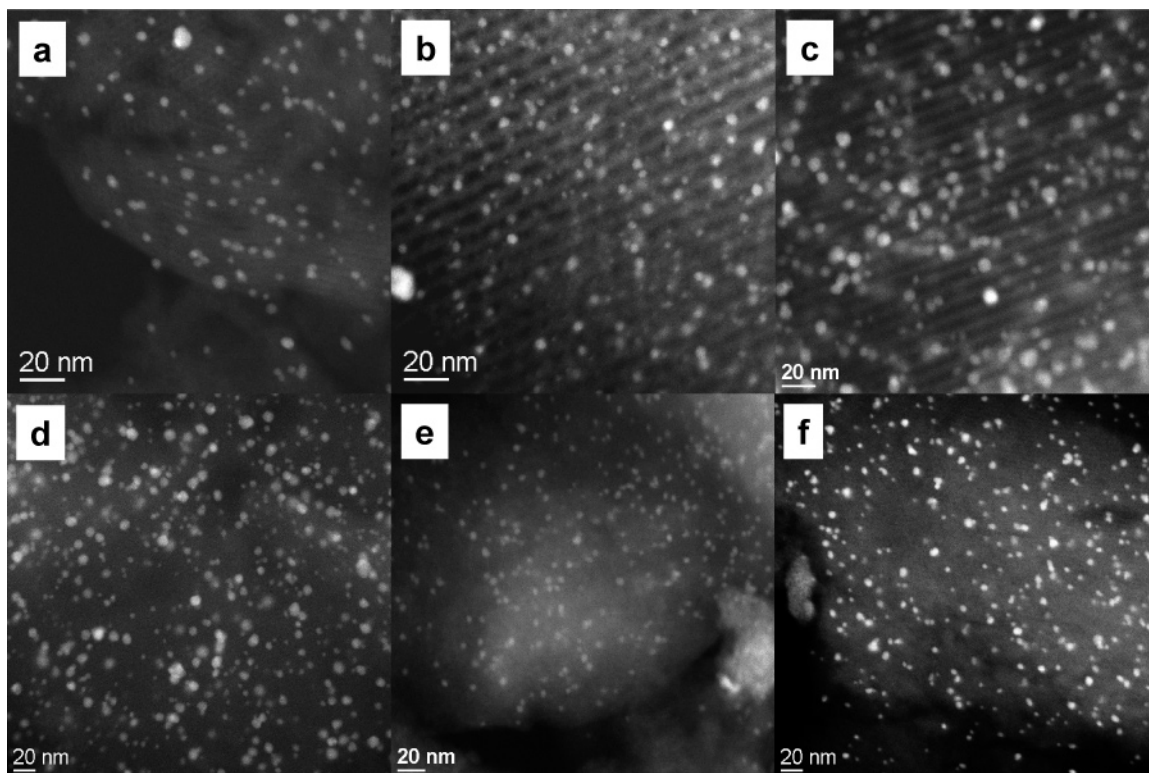


Figure 3. HAADF STEM images of samples after three reaction cycles at temperatures ranging from room temperature to 400 °C. (a) MCM-41, (b) SBA-15, (c) SBA-15/2, (d) HMM-2, (e) SBA-12, and (f) SBA-11.

also calculated from XRD powder patterns using the Scherrer equation. The particle size distributions for these samples are shown in Figure 4 (after reduction) and Figure 5 (after reaction). The surface average diameter (total volume of particles/total surface area of particles) is calculated assuming spherical particles. A broad size distribution gives rise to a larger

difference between the number average and surface average. The volume average should be larger than the surface average, but because the diameter measured by XRD is only 0.75 times the volume average,¹⁵ we can see that the XRD particle sizes are in very good agreement with the surface average diameter calculated using STEM images.

TABLE 1: Summary of Au Average Particle Size and Reactivity

sample	pore structure	surfactant template	pore size (nm)	after reduction in H ₂ at 200 °C		XRD Au average particle size ^c (after reduction) (nm)	after reaction (25–400 °C)		reactivity at 100 °C (mol of CO ₂ /mol of Au)/s × 10 ²
				STEM Au average particle size (after reduction) (nm)	surface average ^b		STEM Au average particle size (after reaction) (nm)	surface average	
NH ₂ -SBA-15/2	2D hexagonal <i>p6mm</i>	P123	6.5	7.2	7.9	6.9	7.8	8.3	4.57
NH ₂ -SBA-15	2D hexagonal <i>p6mm</i>	P123	4.1	4.5	4.8	4.1	5.0	5.5	2.56
NH ₂ -MCM-41	2D hexagonal <i>p6mm</i>	CTAB ^e	2.9	3.9	4.3	3.5	5.9	7.8	1.93
NH ₂ -HMM-2	3D hexagonal <i>P6₃/mmc</i>	ODTMA ^f	2.7	4.7	4.9	4.2	8.2	12.0	5.32
NH ₂ -SBA-12	3D hexagonal <i>P6₃/mmc</i>	Brij 76	2.7	4.2	4.5	3.7	6.0	18.4	2.72
NH ₂ -SBA-11	cubic <i>Pm3n</i>	Brij 56	2.2	6.0	7.3	6.6	6.1	10.9	0.00
				stdev 1.5		stdev 0.4	stdev 1.4		
				stdev 0.8		stdev 0.2	stdev 1.1		
				stdev 0.9		stdev 0.2	stdev 2.2		
				stdev 0.7		stdev 0.2	stdev 3.5		
				stdev 0.8		stdev 0.2	stdev 4.1		
				stdev 1.9		stdev 0.7	stdev 3.0		

^a Number average, $d_N = \sum n_i d_i / \sum n_i$. ^b Surface average, $d_s = \sum n_i d_i^3 / \sum n_i d_i^2$. ^c XRD Au average particle size is calculated by the Scherrer equation. ^d stdev: standard deviation, $\sigma = (\sum (d_i - d_N)^2 / (N - 1))^{1/2}$. ^e CTAB: cetyltrimethylammonium bromide. ^f ODTMA: octadecyltrimethylammonium chloride.

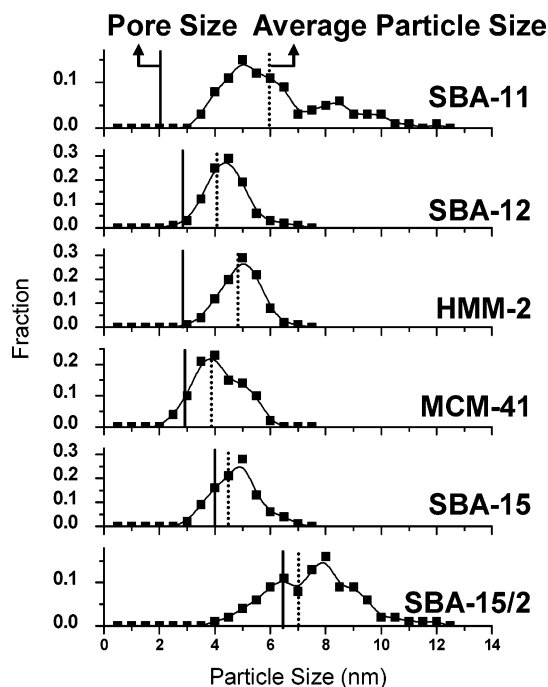


Figure 4. Au particle size distributions after reduction at 200 °C for 2 h in flowing hydrogen. Pore sizes of the samples are calculated using BJH theory. Average Au particle sizes are number averages.

To determine whether Au particles are located inside the pores, the samples were imaged by high-resolution SEM using low accelerating voltage. The low kV ensures that the signal comes from the near surface region. Figures 6–9 show SEM images of MCM-41, SBA-15/2, and SBA-12 samples after reaction. These figures include secondary electron (SE) and backscattered electron (BSE) images at 2 and 5 kV accelerating voltage. The mean free path of the low energy SE electrons ensures that the signal comes from the near-surface region. Hence, the SE image shows primarily topographic contrast, making it difficult to see the metal particles, unless they are large and stand out clearly. Hence, we cannot distinguish any Au particles on the surface of MCM-41 (Figure 6), while we see a few of the largest particles in SBA-15/2 (Figure 8) and almost all of the Au particles can be seen on SBA-12 (Figure 9). On the other hand, the BSE image provides atomic number

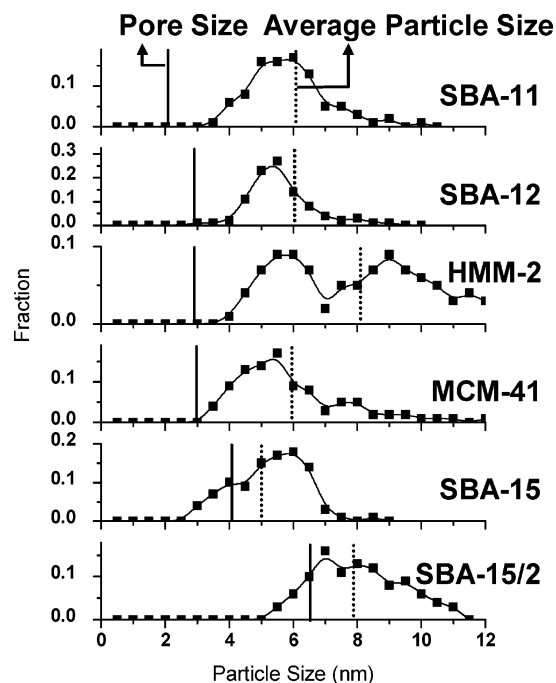


Figure 5. Au particle size distributions after three reaction cycles at temperatures ranging from room temperature to 400 °C. Pore sizes of the samples are calculated using BJH theory. Average Au particle sizes are number averages.

contrast, making it easier to see the Au particles. Backscattered electrons have the same energy as the incident beam, meaning they can come from deeper in the specimen when imaged at 5 kV as compared to 2 kV. Comparison of BSE images at 2 and 5 kV shows clearly whether particles are located deeper in the sample or near the surface. In the sample having 1-D pores, MCM-41 and SBA-15/2, we can clearly see more Au particles at 5 kV than at 2 kV (Figures 6, 7, and 8). In Figure 7, we have arrowed the particles that appear faint at 2 kV but appear bright at 5 kV. Likewise, in Figure 8 we see that most of the particles imaged at 2 kV appear spherical, while at 5 kV we see diffuse and elongated particles, which are located within the pores. Finally, in the sample with 3-D pores, SBA-12 (Figure 9), we see no difference between the images at 2 and 5 kV, suggesting that all of the particles are located on the surface.

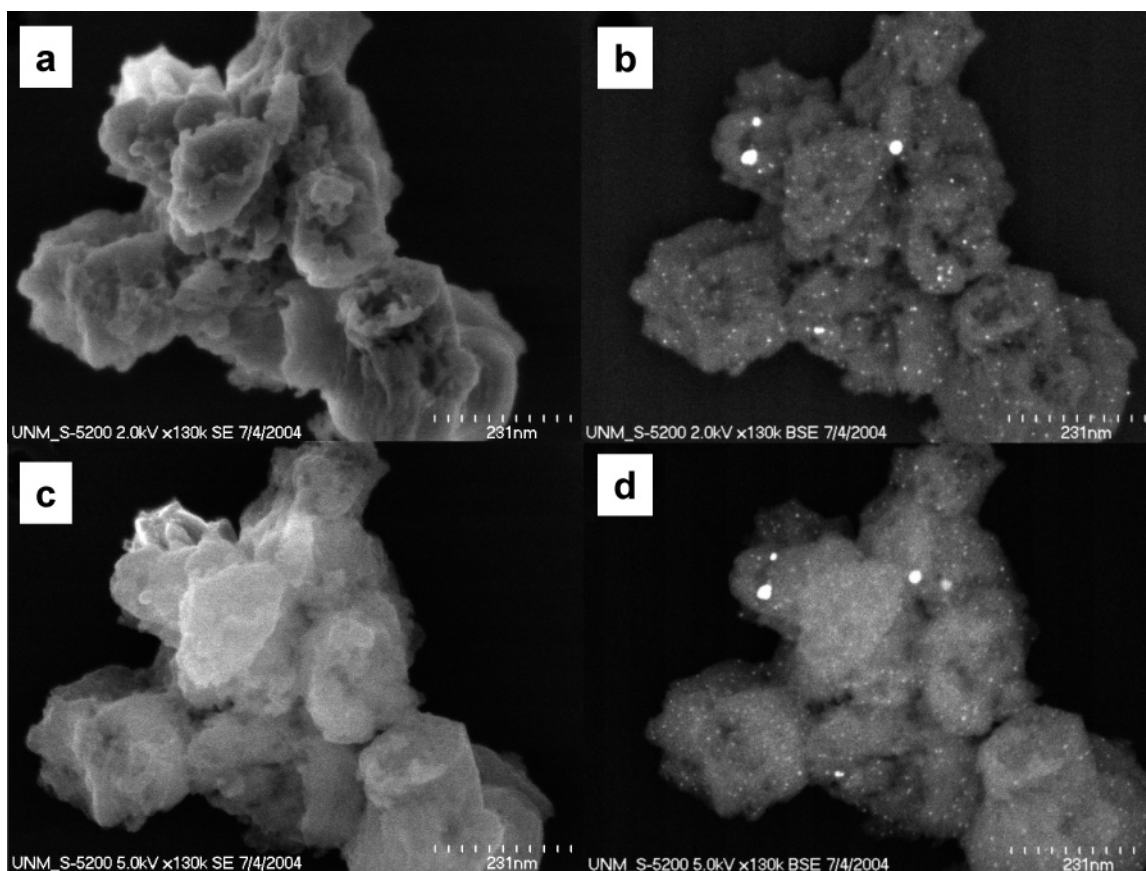


Figure 6. High-resolution SEM images of the MCM-41 sample after reaction. (a) SE image at 2 kV, (b) BSE image at 2 kV, (c) SE image at 5 kV, and (d) BSE image at 5 kV. More of the Au particles can be seen in the BSE images at 5 kV (d) as compared to 2 kV (b).

Discussion

After Reduction at 200 °C in Hydrogen for 2 h. SBA-11, SBA-12, HMM-2, and MCM-41 samples have similar pore sizes in the range of 2.2–2.9 nm but different pore structures. The pore structure of MCM-41 is 2D-hexagonal, SBA-12 and HMM-2 are 3D-hexagonal, while SBA-11 has a cubic pore structure. Particle size distributions for these samples (Figure 4) show that after H₂ reduction at 200 °C, the particles have grown larger than the pore size in each case. Yet for the MCM-41 sample, 15% of the particles are smaller than pore size, while for SBA-11, SBA-12, and HMM-2 samples less than 1% of the particles are smaller than pore size. The average particle size for the MCM-41 sample is less than that for other samples. This observation suggests that sintering was more pronounced for the samples with 3D-hexagonal and cubic pore structures as compared to the 2D-hexagonal pore structure. In the 2D-hexagonal pore structure, the pores are one-dimensional and not connected to each other, while in the 3D-hexagonal and cubic pore structure, the pores are interconnected. We start with the Au particle size of ~1 nm. With such small particles, particle migration as well as Ostwald ripening (emission of adatoms leading to coarsening) are both possible mechanisms.¹ Under these conditions, it seems plausible that Au particles with interconnected pores will sinter faster than those in isolated pores. We therefore conclude that MCM-41 with straight, isolated pores is better able to restrict sintering of the Au particles. However, because the particles all grow larger than the pore size, it is clear that the pore walls are not able to restrain the growth of Au particles. Because most of the Au particles are still inside the pores, we conclude that the pore walls must be deformed as the nanoparticles grow larger than the pore size.

Once the metal particle grows comparable in size to the pore size, we would expect particle migration to slow, so we conclude that much of the sintering must be due to Ostwald ripening.

We next consider the results of sintering of MCM-41, SBA-15, and SBA-15/2 samples, all of which have the 2D-hexagonal pore structure but with differing pore sizes. The pore sizes are 2.9, 4.1, and 6.5 nm for MCM-41, SBA-15, and SBA-15/2 samples, respectively. The particle size distribution shows that as the pore size increases from 2.9 to 6.5 nm, the average particle size also increases from 3.9 to 7.2 nm. With the larger pore diameters, a greater percentage of particles remain smaller than the pore size, 33% versus 15% for the smallest pore size. Thus, smaller pore sizes in the silica lead to a smaller final particle size. This finding agrees with the general observation by Richardson et al.² who also found smaller Ni particles supported on alumina samples having smaller pore size diameters.

After Reaction at 25–400 °C in 20% CO and 10% O₂. The H₂ reduced samples were tested for CO oxidation from 25 to 400 °C at 50 °C intervals. After reaction, there was a further increase in average Au particle size for all of the samples studied. Because most particles were already larger than the pore size, this suggests that Ostwald ripening must be the dominant sintering mechanism under these conditions. The particle size distribution (Figure 5) shows that the percentage of particles smaller than the pore size is less than 1% for MCM-41, HMM-2, SBA-12, and SBA-11 samples, while it is 22% and 18% for SBA-15 and SBA-15/2 samples, respectively. The latter two samples have 1-D pores with the largest pore diameter in this group of samples. It can also be seen that the standard deviation (Table 1) is small for all samples with 1-D pores. The SEM images of these samples shed some light on these

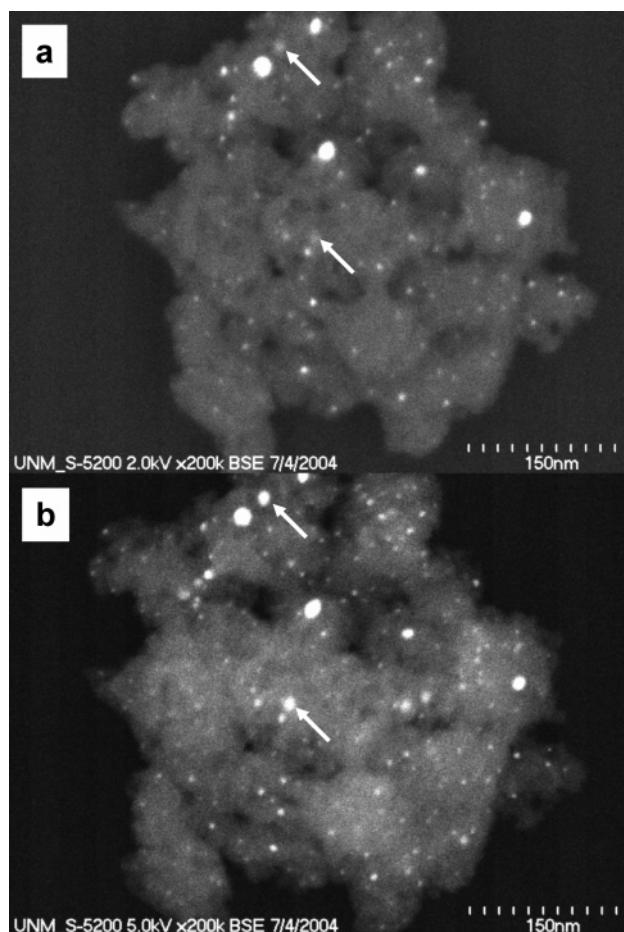


Figure 7. High-resolution SEM images of the MCM-41 sample after reaction. (a) BSE image at 2 kV, (b) BSE image at 5 kV. The arrows show particles that appear faint at 2 kV (deeper than the penetration depth) but appear bright at 5 kV.

observations. The BSE SEM images of SBA-15/2 show the presence of elongated particles, indicating that the pore walls in this silica sample may be strong enough so that the particle growth is confined to the pore space. Such elongated particles were not seen in the other 1-D pore sample, MCM-41. There is a significant difference in the pore wall thickness, with the SBA-15 sample having thicker walls (SBA-15/2, 2.6 nm; SBA-15, 4.8 nm) as compared to MCM-41 (1.0 nm). The thinner walls in the MCM-41 sample are not strong enough to confine the particles to the open pore space, and we suspect that the particles grow to near spherical shapes by crushing the pore walls. Direct evidence by TEM is difficult to obtain because each image represents a projection of a three-dimensional sample on the image plane, and damage in a single pore would not show up because the image contrast represents a large number of pores lined up in the beam direction. On the other hand, with the cubic pore structure in sample SBA-12, it appears that most of the particles after reaction are located outside of the pores, on the surface of the particle.

Mechanism of Sintering: Particle Migration versus Ostwald Ripening. The SEM images allow us to determine the fraction of Au particles that are being retained within the pore structure. This determination is based on the higher penetration of electrons and hence a greater sampling depth for BSE images at 5 kV versus at 2 kV. When the 5 kV image shows many more particles than the 2 kV images, we can infer that these particles must be located deeper within the pore structure of the silica. These SEM images in Figures 6–9 suggest that the

majority of particles in the 1-D pores are retained in the silica while those in 3-D pore structures tend to come out on to the surface. We can interpret these results in terms of the two dominant mechanisms for sintering of the Au particles. Particle migration involves motion of the entire particle and coalescence of two particles to yield a larger one. On the other hand, the Ostwald ripening mechanism involves emission of adatoms and transport from small particles to larger particles. It is clear that particle growth continues even in samples where most of the particles are still located inside the pores. This means Ostwald ripening must be responsible for the continued growth of the particles. However, in the case of the cubic pore structure sample SBA-12, we find most of the particles after reaction are located on the surface. It appears that the 3-D pore architecture may make it easier for the particles to wander out to the silica surface. Hence, particle migration must also contribute, in part, to the observed sintering of the Au nanoparticles in these catalysts. We conclude then that both mechanisms are operative under our conditions.

The presence of large numbers of particles within the pore structure for the samples with 1-D pores, MCM-41 and SBA-15/2, suggests that these types of silicas may be more effective at controlling metal particle sintering by hindering the migration of the particles to the external silica surface. The 3-D pore structure allows the Au particles to migrate more easily to the external surface where they can continue to grow in size. However, to be able to control the particle size, the pore walls need to be strong enough to restrain the particles from crushing the walls and growing larger. None of the silica samples studied here have pore walls strong enough to prevent the Au particles from growing larger than the pore size at the temperatures we have studied. A third parameter that has not been explored in our study is the effect of metal support interactions. Recent work shows that when gold nanoparticles are supported inside the pores of mesoporous silica coated with titanium oxide layers, there is an enhancement of reactivity and improved sintering resistance.¹⁶

Reactivity for CO Oxidation. The reactivities of the reduced samples for CO oxidation at 100 °C are summarized in Table 1. These reactivities are average reactivities after three heating and cooling cycles. The most active samples in our work were SBA-15/2 and HMM-2 with number average Au particle diameters of 7.8 ± 1.4 and 8.2 ± 3.5 nm, respectively. Okumura et al.¹⁷ reported an average Au particle size of 6.6 ± 3.8 nm for their most active Au/SiO₂ catalyst. In our study, we did not see any clear correlation between CO oxidation reactivity and average Au particle size, which could be a result of the differing pore structures in these samples.

Conclusions

Au was deposited on mesoporous silica samples having a range of pore sizes and pore arrangements (2-D hexagonal, 3-D hexagonal, and cubic). The objective was to study the role of pore size and pore structure on the thermal stability of Au particles. These Au catalysts were subjected to H₂ reduction at 200 °C, and then to CO oxidation at temperatures ranging from room temperature to 400 °C. We found that, in each of the samples, the average particle size exceeded the diameter of the silica pores. However, in the samples with 1-D pores (stacked in a 2-D hexagonal structure), we found that the majority of Au particles remained within the pores, despite growing to sizes larger than the pore diameter. In contrast, the Au particles had migrated outside the pores in the silica samples having 3-D interconnected pores. We found clear evidence for particle

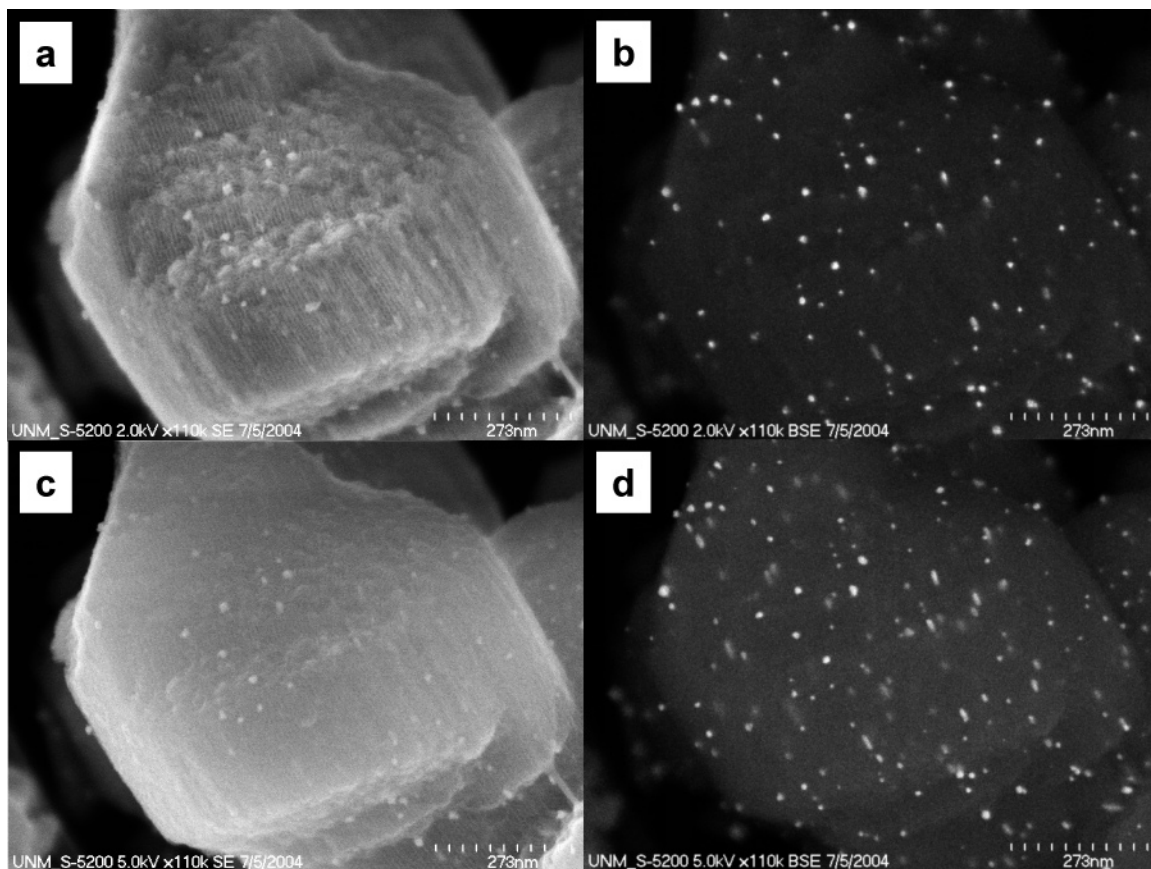


Figure 8. High-resolution SEM images of the SBA-15/2 sample after reaction. (a) SE image at 2 kV, (b) BSE image at 2 kV, (c) SE image at 5 kV, and (d) BSE image at 5 kV. In the BSE images, more Au particles are seen at 5 kV (d) than at 2 kV (b).

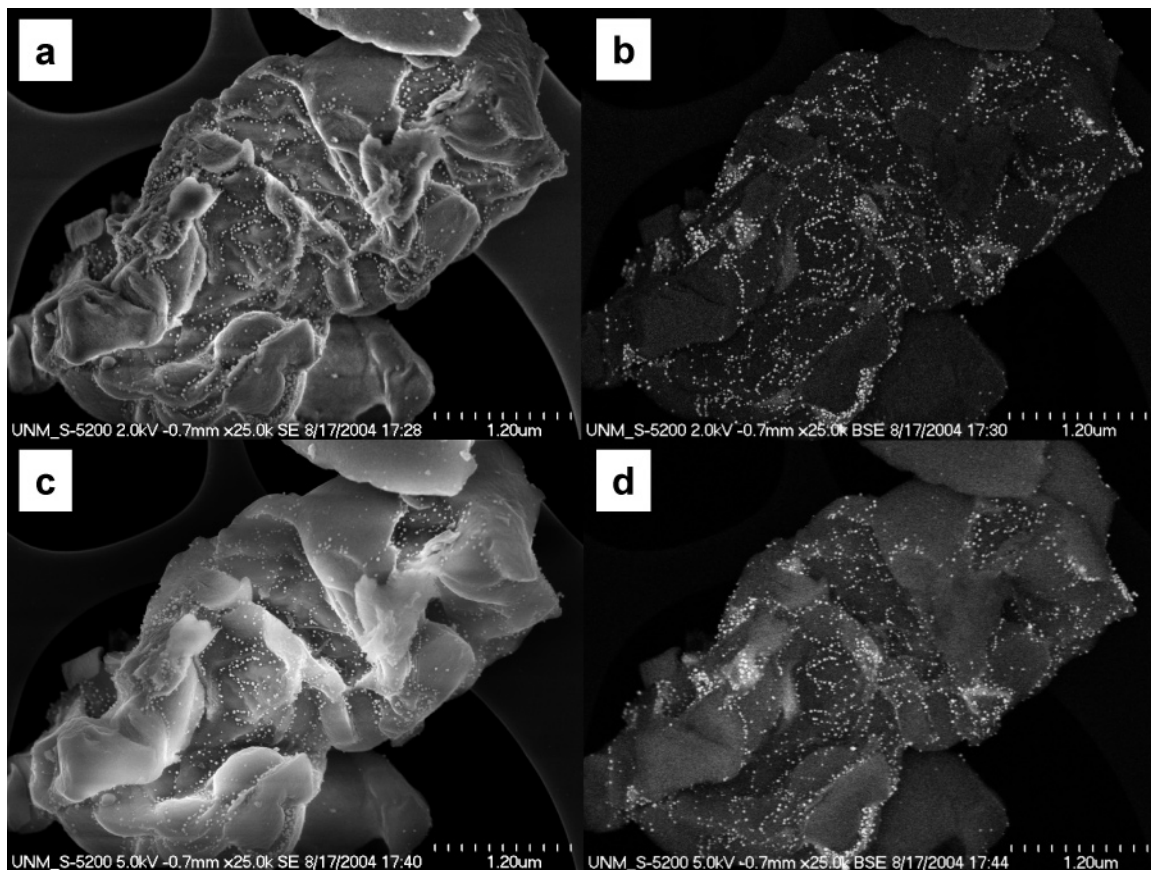


Figure 9. High-resolution SEM images of the SBA-12 sample after reaction. (a) SE image at 2 kV, (b) BSE image at 2 kV, (c) SE image at 5 kV, and (d) BSE image at 5 kV. The Au particles appear to be located on the silica surface because they can be clearly seen even in the SE images (a and c). There is no increase in the number of visible particles when going from 2 to 5 kV.

migration (particles migrating outside the pores) as well as Ostwald ripening (particles growing larger than the pore diameter, but still located within the pores); hence both processes contribute to the observed sintering of Au. Overall, the 3-D pore structures appear to be less effective at limiting the sintering of Au. Among the 2-D structures, the SBA-15 sample with the thickest pore walls was most effective at controlling the growth of the Au particles. In all other samples, the Au particles grew larger than the pore size by destroying the pore walls in the vicinity of the Au particles.

Acknowledgment. We acknowledge financial support from NSF grants CTS 02-10835 and EEC 99-08205, and the Materials Corridor Council supported by the Department of Energy. The characterization facilities used in this work are supported by NSF EPSCOR and NNIN infrastructure grants.

References and Notes

- (1) Bartholomew, C. H. *Appl. Catal., A* **1993**, *107*, 1.
- (2) Richardson, J. T.; Propp, J. L. *J. Catal.* **1986**, *98*, 457.
- (3) Kuo, H. K.; De Angelis, R. J. *J. Catal.* **1981**, *68*, 203.
- (4) Kresge, C. T.; Leonowicz, M. E.; Roth, W. J.; Vartuli, J. C.; Beck, J. S. *Nature* **1992**, *359*, 710.
- (5) Zhao, D.; Huo, Q.; Feng, J.; Chmelka, B. F.; Stucky, G. D. *J. Am. Chem. Soc.* **1998**, *120*, 6024.
- (6) Inagaki, S.; Guan, S.; Fukushima, Y.; Ohsuna, T.; Terasaki, O. *J. Am. Chem. Soc.* **1999**, *121*, 9611.
- (7) Sakamoto, Y.; Kaneda, M.; Terasaki, O.; Zhao, D. Y.; Kim, J. M.; Stucky, G. D.; Shin, H. J.; Ryoo, R. *Nature* **2000**, *408*, 449.
- (8) Kim, J. M.; Sakamoto, Y.; Hwang, Y. K.; Kwon, Y. U.; Terasaki, O.; Park, S. E.; Stucky, G. D. *J. Phys. Chem. B* **2002**, *106*, 2552.
- (9) Shen, S. C.; Kawi, S. *J. Phys. Chem. B* **1999**, *103*, 8870.
- (10) Mokaya, R. *J. Phys. Chem. B* **2000**, *104*, 8279.
- (11) Bore, M. T.; Pham, H. N.; Ward, T. L.; Datye, A. K. *Chem. Commun.* **2004**, *22*, 2620.
- (12) Haruta, M.; Tsubota, S.; Kobayashi, T.; Kageyama, H.; Genet, M. J.; Delmon, B. *J. Catal.* **1993**, *144*, 175.
- (13) Gosh, A.; Patra, C. R.; Mukherjee, P.; Sastry, M.; Kumar, R. *Microporous Mesoporous Mater.* **2003**, *58*, 201.
- (14) Zhu, H.; Lee, B.; Dai, S.; Overbury, S. H. *Langmuir* **2003**, *19*, 3974.
- (15) Matyi, R. J.; Schwartz, L. H.; Butt, J. B. *Catal. Rev.-Sci. Eng.* **1987**, *29*, 41.
- (16) Yan, W. F.; Chen, B.; Mahurin, S. M.; Hagaman, E. W.; Dai, S.; Overbury, S. H. *J. Phys. Chem. B* **2004**, *108*, 2793.
- (17) Okumura, M.; Nakamura, S.; Tsubota, S.; Nakamura, T.; Azuma, M.; Haruta, M. *Catal. Lett.* **1998**, *51*, 53.